

Chapter 5

Deformation Behaviors



5.1 Elastic Moduli

Elastic moduli that characterize the linear relationship between stress and strain express the shape of the potential energy of an atom pair in materials. Hydrogen atoms, located at interstitial sites in the regular lattice, exert stress fields and alter electronic states around them. An expected alteration of the distance or the cohesive force between neighboring host atoms is to appear in the elastic moduli.

Hydrogen effects on Young's modulus of polycrystalline bcc tantalum, niobium, and vanadium were measured from the velocity of 100 kHz elastic wave in wire specimens [1]. Hydrogen charging was done by cathodic electrolysis in 4% H_2SO_4 with small amounts of CS_2 and As_2O_3 . Numerical data of hydrogen contents were not shown, but a linear increase in Young's modulus E with hydrogen content was reported for each metal. The increases in terms of $\Delta E/E$ were 0.07, 0.58, and 0.48% for Ta, Nb, and V, respectively, per 1 at.% of hydrogen. On the contrary, a linear decrease in Young's modulus against the square root of the hydrogen concentration as low as 2.5×10^{-3} was reported for a Ti–Mo alloy accompanying solution softening and expansion of lattice parameter [2].

As described in Chap. 1, the solid solubility of hydrogen in α -iron at room temperature is very low, and expected moduli changes, if any, are also very small. Measurements of the shear modulus of hydrogen-charged polycrystalline α -iron using a torsion pendulum method showed a decrease of about 0.3% of the pendulum frequency at temperatures lower than 200 K [3]. For the experiment, hydrogen was introduced by the electric discharge of wet hydrogen gas. The hydrogen concentration was not exact, but an estimated decrease in the shear modulus of iron by 1 at.% hydrogen was about 8% at 100 K.

5.2 Flow Stress

Lattice distortion around solute hydrogen atoms and the resulted interactions between dislocations and hydrogen, described in Sect. 3.1, may cause the solid solution hardening or softening for the flow stress. However, an exact evaluation is difficult because of low hydrogen concentrations and various trapping lattice defects. For a Ti–Mo alloy cited above [2], the proportional limit and 0.2% proof stress decreased linearly against the square root of hydrogen concentration. For iron and steel, hydrogen effects on the flow stress are fairly complicated depending on materials, deformation stages, and testing conditions. Flow stress is a major controlling factor of mechanical properties, and many early studies addressed the effects of hydrogen on flow stress. Hydrogen effects on the flow stress of iron are not yet conclusive, and Table 5.1 summarizes reported results in the literature [4–15].

5.2.1 Hardening

Hardening by hydrogen is the more general case than softening for commercially pure iron, low-alloyed, and stainless steels tested for bulky specimens at room temperature. For iron single crystals containing about 50 ppm or less carbon, the critical resolved shear stress for yielding increased on {110} <111> slip system in a hydrogen-precharged specimen, while it was almost immune on {112} <111> slip system [4]. The tensile straining, in that case, was at room temperature with strain rates of about 10^{-4} – 10^{-5} /s, using specimens of 2 mm thickness. Hydrogen effects on hardening behaviors varied by carbon contents. For carbon-doped iron single crystals, flow stress on tensile straining in the presence of hydrogen increased with 165 ppm carbon but decreased with 10 ppm [7]. For an intermediate 90 ppm carbon, the flow stress was higher or lower than that of the hydrogen-free specimen according to strain ranges less or larger than 30%, respectively. In the experiments, the tensile straining was at room temperature under cathodic electrolysis, setting the tensile axis near <001>.

For polycrystalline iron containing 10 ppm carbon and ~ 30 μm grain size, the yield and flow stresses increased by hydrogen on tensile straining of specimens of 2 mm thickness [8]. In the experiments, ~ 2 ppm hydrogen was precharged in 0.1 MPa hydrogen gas at 1123 K (850 °C), and tensile tests were at 273 K and 193 K. Strain aging increases flow stress, and a noteworthy fact was that hydrogen enhanced the increase at a strain of less than 5%.

The grain-size dependence of hydrogen effects was also examined in terms of the Hall–Petch relation, i.e., a linear increase in the flow stress against the square root of the grain size, for commercially pure iron of grain size ranging 10–150 μm [9]. Tensile tests were at room temperature under concurrent cathodic hydrogen charging to 2–7 ppm in the average hydrogen concentration. A hydrogen effect appeared on the slope of the Hall–Petch relation. The 0.5% offset stress decreased by hydrogen

Table 5.1 Effects of hydrogen on the flow stress of iron. The residual resistance ratio (RRR) is a measure of the purity of material defined as the ratio of electric resistivity at room temperature and that at 4.2 K [4–15]

	Specimen			H charging	Strain rate (s ⁻¹)	Temperature	Hydrogen effects	References
	Purity	Grain size	Size (t × w)					
1	Decarburized Armco iron (C: 30–50 ppm)	Single crystal	2 × 2 mm	1 N HCl aq + hydrazine 30 A/m ²	3.3×10^{-4} , 3.3×10^{-5}	RT	Hardening for: {110} <111>, Small change for {112} <111>	[4]
2	Zone-refined pure iron	Single crystal	1.5 mmφ	1 N H ₂ SO ₄ + As ₂ O ₃ 40 A/m ²	4×10^{-4}	RT	Softening	[5]
3	Zone-refined pure iron (resistance ratio 4700)	Single crystal	0.4 φ or 0.1 × 1.4	0.1 N CH ₃ OH–H ₂ O–H ₂ SO ₄ 20 or 40 A/m ²	8.3×10^{-4}	200 K	Softening, but hardening in the 3rd work-hardening stage	[6]
4	Zone-refined pure iron (varied C contents)	Single crystal	– TA// <001>	1 N H ₂ SO ₄ + As ₂ O ₃	–	RT	Softening in the 1st and 2nd work-hardening stages. Hardening when C is added	[7]
5	Vacuum melt electrolytic iron	30 μm	2 × 5 mm	1 atm H ₂ , 850 °C × 1 h → liq. N ₂	6×10^{-4}	0–80 °C	Hardening, prominently at ε < 8%	[8]
6	Decarburized Ferrovac E	10–150 μm	–	1 N H ₂ SO ₄ + As 10 A/m ²	6.5×10^{-3}	RT	Enhanced grain-size dependence of proof stress. Hardening for fine grain size less than 30 μm	[9]

(continued)

Table 5.1 (continued)

	Specimen		H charging	Strain rate (s ⁻¹)	Temperature	Hydrogen effects	References
	Purity	Grain size Size (t × w)					
7	Remelt Plastiron (added 0.15%Ti)	10–150 μm	–	6.5 × 10 ⁻³	RT	Softening	[9]
8	Vacuum melt mild steel and pure iron	20 μm	0.06–0.8 × 6 mm	3.3 × 10 ⁻⁵	RT	Hardening, but softening for fine specimen size less than 0.19 mm	[10]
9	Zone-refined pure iron (resistance ratio 3500–6000)	0.3 mm (RRR 3600) 1.0 mm (RRR 5000)	0.4 mmφ	8.3 × 10 ⁻⁵	170–297 K	Softening, but hardening even at 200 k for low-purity iron Enhanced softening at lower strain rate	[11]
10	Zone-refined pure iron (resistance ratio 1800–5000)	0.1 mm (RRR 1800) 0.3 mm (RRR 3600) 1.0 mm (RRR 5000)	0.4 mmφ	8.3 × 10 ⁻⁵	170–297 K	Softening reduced at elevating temperatures. Hardening at room temperature for low-purity iron	[12]

(continued)

Table 5.1 (continued)

	Specimen			H charging	Strain rate (s ⁻¹)	Temperature	Hydrogen effects	References
	Purity	Grain size	Size (t × w)					
11	Zone-refined pure iron + 0.6 at.% Ti Zone-refined pure iron + 0.2 at.% Mo	60–100 μm	0.5 mmφ	<i>ibid</i>	3.3 × 10 ⁻⁵	200–RT	Hardening for Fe–Ti. Hardening at RT but softening at below 0° C for Fe–Mo	[13]
12	Zone-refined pure iron (Resistance ratio 3600–5200)	0.4, 1.0, 2.0 mm	0.4 mmφ	<i>ibid</i>	1.7 × 10 ⁻³ –8.3 × 10 ⁻⁵	170–297 K	Softening reduced by increasing strain rate and current density	[14]
13	Remelt electrolytic iron	Single crystal	TA// <110> (0.1–1.0) × 5 mm	C ₂ H ₅ OH + H ₂ SO ₄ 50 A/m ²	5 × 10 ⁻⁵	195 K	Enhanced softening for smaller specimen size	[15]

for coarse-grain sizes over $\sim 30 \mu\text{m}$ but increased for smaller grain sizes. However, effects of interstitial impurities were present, and for iron with reduced interstitial impurities by adding 0.15% titanium as a getter, the slope of the Hall–Petch relation was almost unaffected, and hydrogen reduced the strength for all grain sizes.

The specimen size is also a vital factor. Effects of hydrogen on the flow stress at room temperature of decarburized rimmed steel containing ~ 40 ppm of carbon vary with of the specimen thickness [10]. Switching on cathodic current for hydrogen charging during tensile straining consistently increased the flow stress for specimens of 0.8 mm in thickness. However, reducing the specimen thickness decreased the flow stress increment, and softening appeared for the thickness of less than 0.20 mm. On the other hand, hardening was always the case for 17Cr steel.

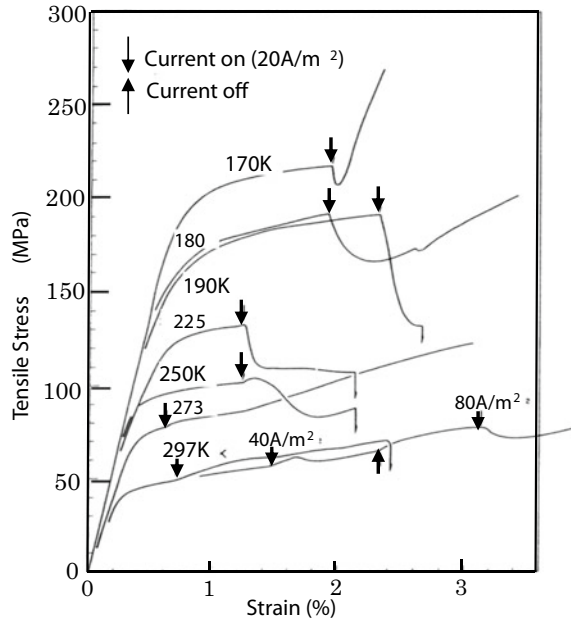
Hardening by hydrogen was also observed for a commercial quenched and tempered steel [8] and a Fe-0.5%Ti alloy [13] on tensile straining at temperatures below room temperature. Another demonstration of hardening was the appearance of two-stage Lüders deformation on tensile straining of commercial 1045 steel [16]. In the experiment, hydrogen was introduced into one-half of the gauge section, and the second-stage Lüders deformation was assigned to the yield in the hydrogen-charged portion.

5.2.2 Softening

Softening by hydrogen generally appears for thin specimens of high-purity iron at temperatures below room temperature. Figure 5.1 [12] shows tensile stress–strain curves of zone-refined high-purity iron specimens as thin as 0.4 mm in diameter tested at low temperatures. Downward and upward arrows indicate switching on and off of cathodic current for hydrogen charging. While hydrogen caused only hardening at room temperature, a gradual decrease of flow stress after a small hump or a rapid decrease appeared at lower test temperatures. The decrease in the flow stress at the start of hydrogen charging was temporal at temperatures lower than 180 K, and the flow stress tended to increase again at 170 K. The initial decrease in the flow stress that appears on hydrogen charging at low temperatures was more prominent for high-purity iron. The amount of softening depends on test conditions. The higher charging current density, the lower strain rate, and the smaller specimen size increased the difference in the flow stresses between the final steady level and before charging [14]. It is to be noted that the microstructures of the coarse-grain specimens were bamboo-like.

Softening by hydrogen was also reported in tensile straining of single-crystal iron specimens, as thick as 3 mm in diameter, within the easy glide region under continuous hydrogen charging at room temperature [17]. Slip markings on the specimen surface were finer for hydrogen-charged specimens than those of the hydrogen-free ones. The work-hardening rate soon after yielding increased in the presence of hydrogen, and shear stress exceeded that of hydrogen-free specimens, i.e., softening turned to hardening. However, the critical resolved shear stress for yielding

Fig. 5.1 Effects of cathodic polarization on tensile curves of pure iron specimens at different temperatures (Matsui et al. [12])

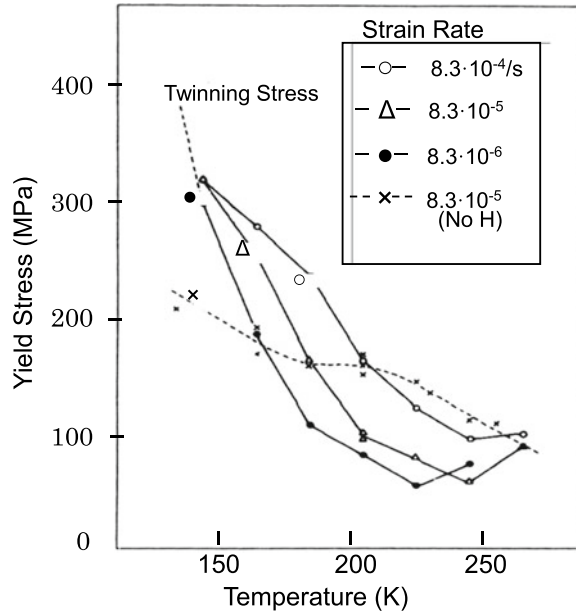


was almost the same for specimens with and without hydrogen charging. Softening also appeared over a wide strain range at 200 K for a single-crystal iron specimen of 2 mm in thickness, but a polycrystalline iron showed hardening in small strain of less than 5% [18].

Softening by hydrogen is prominent for low strain rates. Figure 5.2 [11] shows the temperature dependence of the yield stress of high-purity iron tested at different strain rates. For the experiments, the specimens of 0.4 mm in diameter were given 1–2% prestrain and cathodic hydrogen precharging. The yield stress increased with decreasing temperature and exceeded the yield stress of the hydrogen-free specimens, i.e., turned to hardening by hydrogen at low temperatures. Prestrain introduced fresh dislocations in specimens, and aging of prestrained and hydrogen-precharged specimens at room temperature diminished hydrogen effects on the yield stress, or rather showed hardening at 200 K, even at the strain rate as low as $8 \times 10^{-5}/s$ [11].

Prominent softening by hydrogen was reported earlier as a pronounced decrease of torque in torsion tests of mild steel tubes [19]. The specimen was a tube of 2 mm in wall thickness and 20 mm in outer diameter. The test was conducted at room temperature, and hydrogen was introduced by immersing the specimen in 5% H_2SO_4 with small additions of poisons. The observed softening, coupled with transitions of fractographic feature presented in Sect. 7.2.5, was a basis of the hydrogen-assisted cracking (HAC) mechanism of hydrogen embrittlement, described in Sect. 10.2.

Fig. 5.2 Yield stress of prestrained and hydrogen-precharged iron at different strain rates and temperatures. The broken line is for specimens without hydrogen (Moriya et al. [11])



5.2.3 Explanations of Experimental Results

As described above, observed hydrogen effects on flow stress are complicated, depending on the material purity, grain size, specimen size, testing temperature, strain rate, and hydrogen fugacity. For focusing discussion, dislocation dynamics is the primary player in the flow stress, and the applied flow stress τ_{app} must overcome the sum of the intrinsic flow stress τ_0 and the internal stress τ_{int} , i.e.,

$$\tau_{app} = \tau_0 + \tau_{int}. \quad (5.1)$$

τ_{int} is composed of short- and long-range stress fields. Further, under a given strain rate $\dot{\epsilon}$, τ_{app} keeps the average dislocation velocity \bar{v} that satisfies

$$\dot{\epsilon} = b\rho\bar{v}, \quad (5.2)$$

where b is the Burgers vector and ρ is the dislocation density. Any term in Eq. (5.1) and (5.2) is a candidate to tolerate hydrogen effects, not necessarily limited to the intrinsic mobility of dislocations. A fact to be noticed is that a decrease in the flow stress is remarkable at switching on hydrogen charging in a transient state, i.e., during a dynamic state of the specimen.

Concerning the mechanism of hydrogen embrittlement, softening, rather than hardening, has been given much attention as hydrogen effects, as described in Sect. 10.2. Discussion on the effects of softening has been in the following aspects:

(1) interactions of hydrogen with dislocations, (2) the increase in the density of mobile dislocations, and (3) the formation of damage in near-surface areas. The last aspect is vital in experiments using cathodic electrolysis under substantially high hydrogen fugacity. The authors of the original papers interpreted their results briefly as follows:

(a) Kink-pair formation

The motion of screw dislocations dominates plastic deformation after preyield strain for iron single crystal at low temperatures. The formation of a kink and its sideward movement energetically favors the slip of a dislocation line. The Peierls potential for screw dislocations in bcc metals is high, and strain rate is controlled by the kink-pair formation and the side-way movement of kinks. To explain softening observed for high-purity iron, Matsui et al. postulated that hydrogen enters the dislocation core and modifies the core structure to increase the double-kink nucleation rate [12]. A prompt response of the flow stress to cathodic polarization was ascribed to the hydrogen transportation by moving dislocations.

Characteristic experimental conditions employed by Matsui et al. were high hydrogen fugacity, extremely high purity, and coarse-grain thin specimens. High concentrations of hydrogen far exceeding equilibrium may exhibit solid solution hardening or softening in similar ways as carbon and nitrogen play their role. However, Matsui et al. ruled out this possibility from tests at temperatures at which hydrogen was mobile together with dislocations. They assumed that interactions between hydrogen and impurities cause hardening at and above 273 K in impure specimens containing dissolved impurities of comparable concentrations as hydrogen. First-principles calculations for hydrogen interactions with the core of screw dislocations and their role in the mobility of dislocations are presented in Sects. 3.1.2 and 5.5.2, respectively.

(b) Long-range internal stress

On the other hand, Lunarska et al. suggested that softening by hydrogen in the easy glide region at room temperature was due to long-range internal stress rather than double-kink formation because the critical resolved shear stress for yielding was unaffected by hydrogen charging [17]. The proposed mechanism was that hydrogen segregation around dislocations lowered elastic interactions between dislocations. On the other hand, fine slip markings and higher work-hardening rates leading to hardening in Stage III feature hydrogen effects. Lunarska et al. also suggested the formation of some obstacles against dislocation motion.

Hydrogen effects enhancing the mobility of dislocations are also discussed concerning elastic field shielding by hydrogen in Sect. 5.5.1 concerning direct observations by transmission electron microscopy. Hydrogen-enhanced strain localization (HELP) associated with the formation of defects is described in Sect. 7.2.3, concerning fractographic features.

(c) Surface effects

High hydrogen fugacity eventually induces surface damage, and some blisters appear on the surface of hydrogen-charged specimens [12]. Oriani and Josephic noticed that the generation of blisters or microvoids causes softening by reducing localized stress at the sites and thus increasing the effective stress [16]. They also noticed that the surface of microvoids might facilitate plastic deformation by serving as an additional source and sink of dislocations, increasing the number of mobile dislocations and reducing the number of dislocation pileups. On the other hand, for the hardening effects of hydrogen, Oriani and Josephic proposed that hydrogen reduces stacking fault energy that impedes cross-slipping. Suppression of the dislocation nucleation from grain boundaries and their ledges was another mechanism Oriani and Josephic proposed for hardening.

The specimen-size dependence of softening [10] supports the idea that surface effects originate in flaws induced by hydrogen charging. However, softening appeared even under mild hydrogen-charging conditions by which the formation of blisters is unlikely [11]. Changes in stress–strain curves associated with switching on and off charging current are too complicated to ascribe simply to the formation of blisters or voids. A viable viewpoint, though so far not paid so much attention to, on the flow stress under concurrent electrolysis is the decrease in surface energy due to the hydrogen adsorption on the surface. Surface effects are particularly critical in experiments using thin specimens. As described in the following sections, surface effects likely operate in stress relaxation, creep, and dislocation mobility under in situ transmission electron microscopy. The generation of dislocations from the surface, the release of dislocation pinning on the surface, and associated changes in internal dislocation structures must be considered.

(d) Point lattice defects

An indispensable aspect of hydrogen functions associated with the movement of dislocations is the creation of point defects. Moving dislocations multiply, and screw dislocations gliding on a slip plane generate jogs by intersecting screw dislocations on other slip planes. Transmission electron microscopy revealed large jogs, forming dipoles of edge dislocations in a single crystal of 3% Si iron [20], and the formation of tangles and cells of dislocations resulting from mutual interactions of dislocations in iron single crystals [21]. Interactions of dislocations with other lattice defects are vital factors controlling dislocation structures as well as flow stress. Interactions of hydrogen with lattice defects created by moving dislocations are crucial, particularly in *areas where the density of dislocations is substantial*, rather than in elementary slip processes of dislocations. Interactions of hydrogen with vacancies created by dragging jog are described in Sect. 3.2.3.

5.3 Stress Relaxation and Creep

5.3.1 Stress Relaxation

Stress relaxation is a partial release of external stress under a constant-strain condition. An example of stress relaxation in engineering practice is the loss of compacting force in prestressed steel structures. Stress relaxation eventually leads to fracture, and delayed fracture of steel components stressed at constant displacement in corrosive environments is a case where hydrogen-assisted stress relaxation occurs.

Dislocation configurations, forming under rising stress, turn toward stable structures when the increase in stress is stopped. At a constant-strain condition, the macroscopic strain rate is zero, i.e.,

$$\varepsilon = \varepsilon_e + \varepsilon_p \text{ const}, \quad (5.3)$$

then

$$\dot{\varepsilon}_p = -\dot{\varepsilon}_e = -\frac{\dot{\sigma}_e}{E}, \quad (5.4)$$

where suffixes e and p denote elastic and plastic, respectively, and E is Young's modulus. Equation (5.4) implies that the plastic strain rate associated with the rearrangement of dislocations appears as a decrease in elastic stress rate. Stress relaxation originates in microplasticity, a measure of the stability of microstructures, particularly dislocation configurations. The relaxation rate is very susceptible to temperature variation, and careful temperature control is necessary for stress-relaxation measurements.

The plastic strain-rate Eq. (5.2) is from the dislocation theory of plasticity. When the viscous flow model of dislocations [22] is employed, the average dislocation velocity \bar{v} is expressed as

$$\bar{v} = A(\tau - \tau_i)^m, \quad (5.5)$$

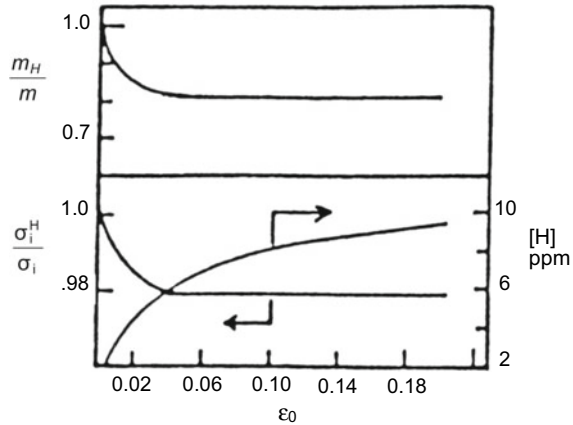
where A is the average velocity at unit effective stress, τ is the applied shear stress, τ_i is the internal shear stress, and m is the dislocation velocity-stress exponent. Equation (5.2) is written using Eqs. (5.4) and (5.5) as

$$\dot{\varepsilon}_p = -K\rho(\tau - \tau_i)^m, \quad (5.6)$$

where K is a constant [23]. Then, hydrogen effects in stress relaxation are related to the density of mobile dislocations, the magnitude of internal stress, and m .

Hydrogen enhances stress relaxation. Stress relaxation of a zone-refined pure iron in the uniform elongation region shows a substantial enhancement when cathodic

Fig. 5.3 Deformation parameters in Eq. (5.5) for coarse-grain pure iron at stress-relaxation tests from different initial strains ε_0 with and without hydrogen charging. Hydrogen-charging current is 3.8 mA/cm² (Lunarska [24])



hydrogen charging is applied [24]. Figure 5.3 [24] shows hydrogen effects on deformation parameters in Eq. (5.5) obtained by stress-relaxation experiments for coarse-grain pure iron at room temperature. Stress relaxation started at different initial tensile strains ε_0 , and hydrogen charging was applied some 1.5–5 min after the start of stress relaxation, using cathodic electrolysis in poisoned 1 N H₂SO₄ at a current density of 20 to 170 A/m². Figure 5.3 indicates that hydrogen reduces internal stress and the dislocation velocity-stress exponent m in Eq. (5.5). Hydrogen fugacity in that experiment was substantially high, while the data collection was before the formation of blisters. A reduction in the current density or interruption of hydrogen charging again increased the load, and the restart of the cross-head movement accompanied a jump-like increase in the load. Similar hydrogen effects in stress relaxation were observed for many types of iron and steel.

Figure 5.4 [10] shows the effects of hydrogen charging to enhance stress relaxation in decarburized rimmed and 17Cr steel. Cathodic polarization was applied during stress relaxation at a constant strain of 4%. The thickness of the specimen was 0.8 mm, but the enhancement was more prominent for thinner specimens [10], similarly to the flow stress on tensile straining.

The magnitude of the charging current density is related to hydrogen fugacity that determines the solid solubility of hydrogen (Sect. 2.1.1). Oriani and Josephic showed a threshold in the input hydrogen fugacity, i.e., some critical hydrogen-charging current density, to induce an abrupt increase in the relaxation rate [25]. The threshold fugacity was higher for a higher initial strain to start stress relaxation. On the other hand, at initial strain below a certain amount, a well-defined effect by hydrogen was not discernible on the slope of the relaxation curve. The experiments were conducted for AISI 1045 steel sheet 0.25 mm in thickness at room temperature, carefully controlling test temperatures. Oriani and Josephic used poisoned 0.1 N NaOH for electrolyte at very low current density, and the estimated threshold fugacity was several MPa. On the other hand, most preceding flow stress and stress-relaxation experiments employed hydrogen charging under substantially high fugacity. Oriani

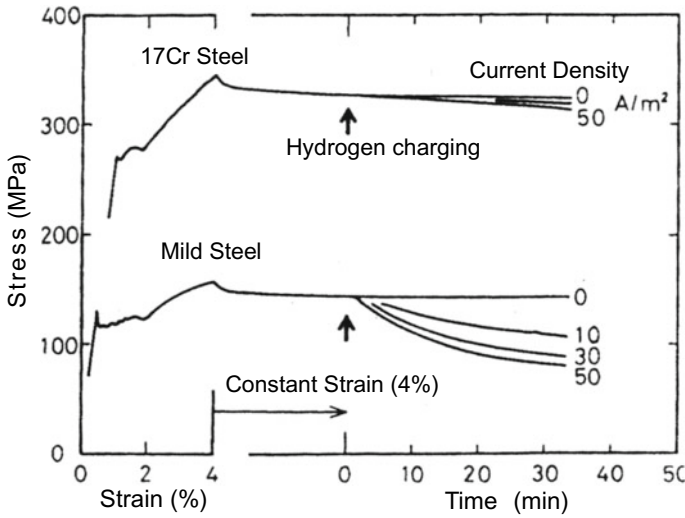


Fig. 5.4 Stress-relaxation curves of mild steel and 17Cr steel specimens started at constant strain of 4%. Cathodic electrolysis was applied in the course of stress relaxation (Asano et al. [10]. Reprinted with permission from Japan Inst. Metals)

and Josephic discussed the mechanism from the viewpoint of the hydrogen-assisted nucleation and growth of microvoids due to decohesion of atomic bonds.

An enhancement in stress relaxation appears not only on hydrogen charging during stress relaxation but also by precharged hydrogen. Figure 5.5 [26] shows stress-relaxation curves of 0.37%C–0.6%Si–1.0%Mo–0.5%Cr–0.54 V martensitic steel tempered at 550 °C (823 K) and 650 °C (923 K). Secondary hardening due to the precipitation of fine vanadium carbides by tempering at 923 K, coupled with advanced recovery of martensite, gave the same tensile strength of 1470 MPa as that for specimens tempered at 823 K. Hydrogen precharging was conducted in a mild condition using cathodic electrolysis in a 3% NaCl + 3 g/l NH₄SCN solution at a current density of 5 A/m². The specimens were 2 mm thick, and stress relaxation at 28 ± 0.5 °C (301 ± 0.5 K) started by stopping tensile straining at 60% of the ultimate tensile strength. Enhancement of stress relaxation by hydrogen was observed for both tempering temperatures, but tempering at 923 K substantially reduced the extent of relaxation. High tempering temperatures and homogeneous distributions of vanadium carbides stabilize martensite microstructures. The stable and homogeneous structures suppress strain localization and rearrangement, reducing additional plastic strain at stress relaxation.

Stress relaxation that occurs on stopping the stress rise to keep a constant displacement is similar to a decrease in the flow stress on tensile straining by switching on hydrogen charging, both representing breakdown of dynamic equilibrium. The breakdown is associated with microplasticity. Hydrogen enhancement of stress relaxation

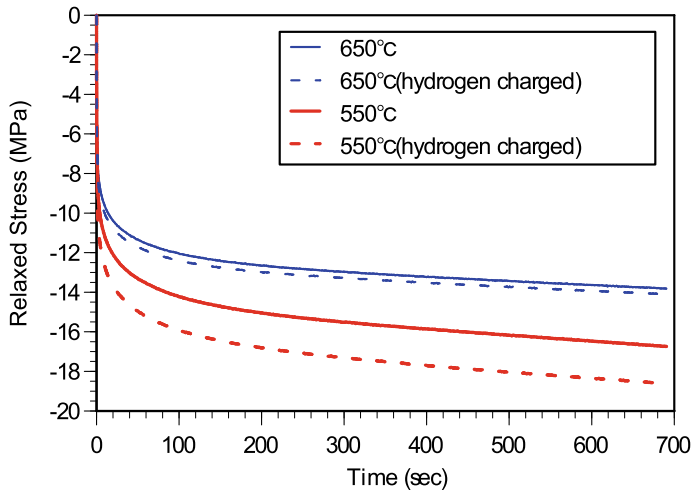


Fig. 5.5 Effects of hydrogen precharging on stress-relaxation curves of Mo–V martensitic steel specimens tempered at 550 (823 K) and 650 °C (923 K). The initial stress is 0.6 of the tensile strength, and the test temperature is 28 ± 0.5 °C. (Nagumo et al. [26])

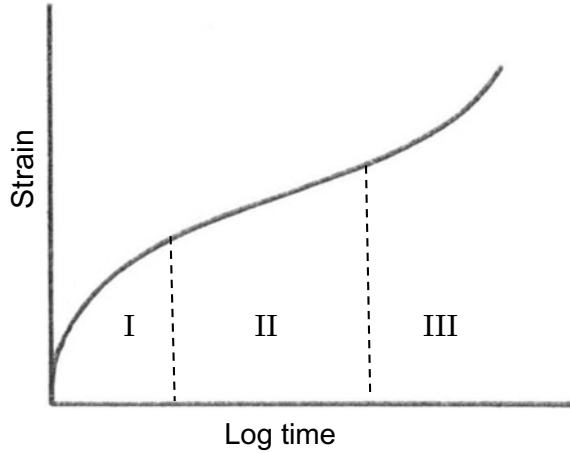
implies a concern of hydrogen with the origin of microplasticity, presumably a change in internal stress fields.

A noteworthy fact concerning the relevance of stress relaxation to hydrogen embrittlement was that tempering of the Mo–V steel at 923 K improved the resistance to delayed fracture compared with tempering at 823 K [26]. The relevance of stress-relaxation rates to the susceptibilities to delayed fracture is likely a general feature for steel of similar strength levels or chemical compositions. Early studies revealed a high resistance to delayed fracture and a very small stress relaxation in an 18Ni maraging steel [27]. A correlation between stress-relaxation rate and the time to fracture in delayed fracture tests also existed for low-carbon martensitic steels [28]. The relevance of stress relaxation in Fig. 5.5 to hydrogen embrittlement for the Mo–V martensitic steel is described in Sect. 6.4.2 about Fig. 6.28 and in Sect. 8.1.2 about Fig. 8.5.

5.3.2 Creep

Creep is time-dependent plasticity under constant load or stress and is particularly important for the high-temperature engineering life of materials. At elevated temperatures, grain-boundary sliding or diffusion of vacancies is the primary origin of creep failure. Creep strain is normally minimal at room temperature, but delayed fracture under constant applied stress is a phenomenon accompanying creep. Various mechanisms likely operate according to types of materials, applied stress, and temperatures

Fig. 5.6 Schematic illustration of three stages in creep curve



[29]. Internal stress and obstacles against slip oppose the dislocation motion induced by external stress. However, thermal energy activates dislocations or other elements equilibrated under applied stress, causing microplasticity.

The general form of the creep curve is schematically shown in Fig. 5.6, and it depends on temperature and applied stress. Three stages generally compose the creep curve: the transient creep stage of decelerating flow, the steady-state creep of a constant minimum rate, and, eventually at high temperatures, the accelerating flow stage that ends in fracture. The exhaustion theory of transient creep is that each element is thermally activated only once by characteristic activation stress, contributing to plastic strain [29]. The creep rate in the transient and steady-state stages is expressed as

$$\dot{\epsilon} = At^{-n}, \quad (5.7)$$

where A and n are constants and $0 < n < 1$.

Creep is a thermally activated process, and the steady-state creep rate strongly increases with temperature. The creep rate over a small range of stress is expressed in terms of the activation energy of dislocation movement in the form of

$$\dot{\epsilon} = K \exp\left(-\frac{U - b\sigma}{RT}\right), \quad (5.8)$$

where K , U , and b are constants. Cottrell derived a refined form of the activation energy, considering dislocation movement passing through closely spaced obstacles, like dislocation forests [30]. However, studies in the following about hydrogen effects were before this consideration.

Hydrogen effects on the density, mobility, and barriers to the movement of mobile dislocations appear on creep behaviors, while experiments on this matter are not

many. Creep rates are higher for higher hydrogen concentrations, similarly to the stress-relaxation test shown in Fig. 5.4. During creep deformation of a single-crystal specimen of pure iron at 200 K, the creep rate was immune to a sudden application of cathodic potential when the potential was low. An increase in the applied potential accelerated the creep rate, initially gradually, then rapidly, and finally to a nearly steady state [18]. In the experiments by Park et al., the thickness of the specimens was 0.8 mm, and the applied stress was 60% of the yield stress.

Hydrogen effects were more prominent at higher current densities and stress levels, but the acceleration decreased with increasing temperature and was insignificant at room temperature. Turn-off the potential reduced the creep rate in a few minutes to the initial value before cathodic charging. Such temperature dependence of the accelerated creep rate is similar to softening of the flow stress shown in Fig. 5.1.

The threshold fugacity for accelerating creep rate was also found by Oriani and Josephic with spheroidized AISI 1040 steel [31] by a similar method as used for stress relaxation [25]. The wire specimen was 0.12 mm in diameter, and hydrogen charging was by cathodic electrolysis in poisoned 0.1 N NaOH aqueous solution at room temperature. The creep rate at room temperature increased abruptly on applying cathodic potential above a critical value. The increase then decelerated following the form of

$$\varepsilon - \varepsilon_0 = k \ln(t - t_0). \quad (5.9)$$

Shut off the charging current immediately and markedly raised the creep rate to a maximum, followed by a decrease. Oriani and Josephic inferred the function of hydrogen similar to that in stress relaxation [25], i.e., the reduction in internal stress due to the nucleation and growth of microvoids induced by a hydrogen-reduced cohesive strength, but no supporting observations.

The contribution of vacancies to creep becomes significant with elevating temperatures. If hydrogen increases the density of vacancies, as described in Sect. 3.2.3.1, hydrogen must increase creep rate. The creep rate at 736–1200 K of a Pd wire of 0.1 mm in diameter was about six times higher in a 0.1 MPa H₂ atmosphere than in an Ar atmosphere of the same pressure [32]. Hydrogen reduced the creep activation energy from 38.6 ± 1.9 kJ/mol in Ar gas to 30.0 ± 1.5 kJ/mol in H₂ gas. The mechanism of the observed creep was ascribed to grain-boundary diffusion of Pd atoms, while the hydrogen effect on the diffusion of Pd atoms was out of the discussion.

5.3.3 Implications of Surface Effects

The effects of hydrogen on stress relaxation and creep have been discussed mostly regarding hydrogen interactions with moving dislocations and surface damage induced by a high hydrogen fugacity. Hydrogen is introduced into metals by cathodic polarization, but the creep rate also increases by anodic polarization. Figure 5.7 [33] compares the creep curves of a thin copper wire for (a) anodic and (b) cathodic

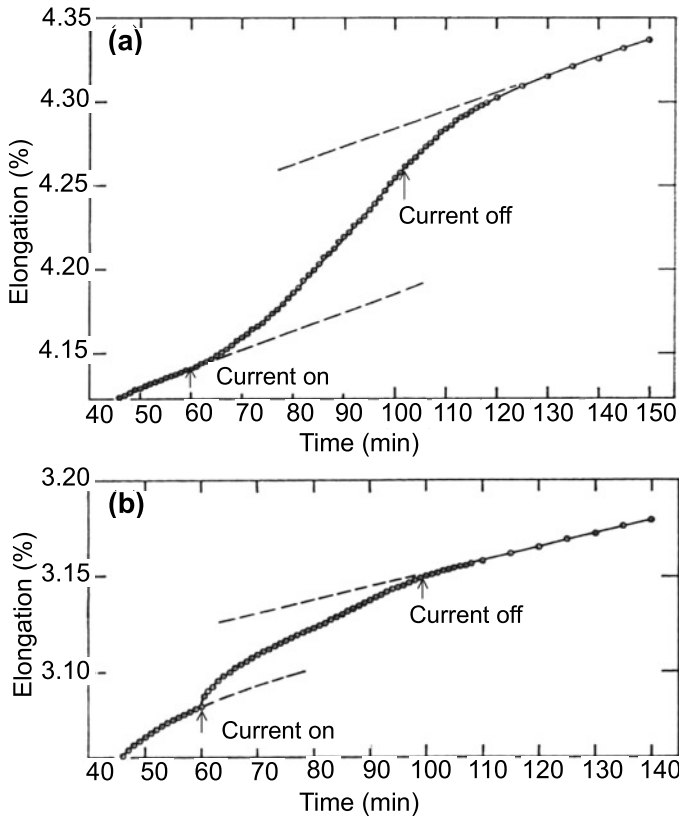


Fig. 5.7 Effects of polarization on creep curves of Cu wire at room temperature. The diameter of wires is 0.27 mm, and the applied stress is 90 MPa. (a) Anodic polarization and (b) cathodic polarization (Revie et al. [33])

polarizations. The average grain size was about 20 μm , and the diameter of the wire was 0.27 mm. The electrolyte was an aqueous acetate buffer solution of pH 3.7 at $298 \pm 0.5 \text{ K}$ ($25 \pm 0.5 \text{ }^\circ\text{C}$), and the current density was 9 A/m^2 . Both cathodic and anodic polarizations increased the creep rate. Anodic polarization gradually increased the creep rate, and shutting off the current decreased the rate to a level similar to before the polarization application. On the other hand, cathodic polarization also increased the creep rate to the same order as anodic polarization. Still, the increase in creep rate was abrupt on the application of polarization.

The increase in the creep rate by both anodic and cathodic polarizations implies that some factors other than hydrogen affect the creep rate associated with chemical reactions on the specimen surface. On anodic polarization, the estimated thinning of the wire was not significant. Revie and Uhlig [33] ascribed the observed lag in the creep response to a diffusional process of vacancies created very near the metal surface associated with the metal dissolution, and Jones later systematically discussed

concerning stress corrosion cracking [34]. Divacancies diffusing from the surface were assumed to interact with sessile dislocations causing climb under applied stress.

On the other hand, cathodic polarization causes an abrupt increase in creep rate, a very small current density of 0.1 A/m^2 resulting in a marked increase in creep rate compared with anodic polarization. Revie and Uhlig ascribed the effect to the reduction of surface energy. Generated hydrogen by cathodic electrolysis adsorbs on the specimen surface, preceding the entry into the bulk. The Gibbs adsorption isotherm gives the change in the surface energy, $d\gamma$, of metals caused by a change of the chemical potential, $d\mu$, of an adsorbed phase. For the adsorption at temperature T and pressure p ,

$$\begin{aligned} d\gamma &= -\Gamma d\mu \\ &= -\Gamma k_B T \ln p, \end{aligned} \quad (5.10)$$

where Γ is the number of molecules adsorbed per unit area and k_B is the Boltzmann constant [35]. For the Langmuir adsorption, i.e., monolayer adsorption, of dissociated atoms of diatomic molecules, γ is expressed as

$$\gamma = \gamma_0 - 2\Gamma_s k_B T \ln[1 + (Ap)^{1/2}], \quad (5.11)$$

where γ_0 is the surface energy without adsorption, Γ_s is the saturation value of Γ , and A is a constant.

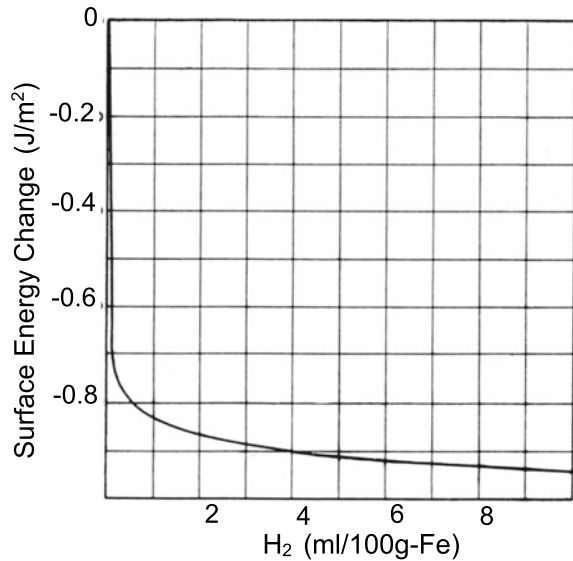
Petch calculated the reduction of γ of α -iron caused by hydrogen adsorption on the crack surface at room temperature. Details of the calculation are described in Sect. 9.2, and the results are shown in Fig. 5.8 [35]. Reduction in surface energy facilitates the formation of new surfaces, and the idea is viable as a mechanism of hydrogen embrittlement. The magnitude of γ_0 is about 2 J/m^2 , and the fractional reduction of γ shown in Fig. 5.8 is substantial even for very low hydrogen concentrations.

Revie and Uhlig postulated that the reduction in the surface energy facilitated slip step formations on the metal surface [36]. The ease of the slip step formation is feasible in grains facing the surface, and the idea is consistent with the higher acceleration of creep rate for larger grain-size specimens. The idea is also compatible with the fact that the application of cathodic polarization causes a sudden response of creep rate.

If the reduction in the surface energy due to adsorbed hydrogen affected the creep rate, it also should play a role in stress relaxation. Changing stress states at the surface should alter the balance of internal stress states, inducing extra plastic strain. From this notion, the additional plasticity is not a consequence of some direct interactions between hydrogen and dislocations within the bulk phase. In this context, the abrupt drop of the flow stress associated with cathodic polarization on tensile straining, shown in Fig. 5.1, might be ascribed to a decrease in surface energy.

However, Fig. 5.5 demonstrates the effects of internal, not externally introduced, hydrogen on stress relaxation. It implies that surface effects, if any, are not the sole

Fig. 5.8 Decrease in the surface energy of iron by adsorption of hydrogen (Petch [35])



origin of hydrogen effects on creep and stress relaxation. Another viable mechanism is interactions between hydrogen and strain-induced vacancies. Vacancy formation associated with cathodic electrolysis or dissociation of water molecules at the surface of pure aluminum was observed by Birnbaum et al. [36]. Small-angle X-ray scattering and measurements of lattice parameters showed the formation of hydrogen-vacancy complexes clustered into platelets lying on the {111} planes. Candidate origins of vacancies are interactions of moving dislocations and possible products on the surface in the case of anodic polarization.

5.4 Direct Observation of Dislocation Activity

The decrease in flow stress in Fig. 5.1 and the enhanced stress relaxation in Figs. 5.4 and 5.5 led to the idea that hydrogen enhances plasticity. Strong support for the notion has been obtained using in situ environmental cell transmission electron microscopy (TEM). The first observation was for iron foils stretched to a constant displacement in an equipped environmental cell, initially in a vacuum and successively in hydrogen gas [37]. Increasing the hydrogen gas pressure up to 35 kPa increased the velocity of screw dislocations, and removing the gas promptly decreased dislocation velocity to the initial value in a vacuum. Similar results were observed for various metals and alloys of bcc, fcc, and hcp structures [38].

For high-purity aluminum, introducing hydrogen increased the length of screw components of dislocations at the intersection of two slip planes and decreased the length of mostly edge components [39]. It was deduced then that dislocation pinning

by hydrogen stabilized edge segments of dislocations, reducing the tendency to cross-slipping [39]. For a nickel, detailed observations exhibited hydrogen effects to increase the dislocation velocity and the generation rate of both isolated and tangled dislocations [40]. The increase in dislocation velocity was observed for dislocations lying in tangles and emanating from crack tips, and the origin was ascribed to a volumetric rather than a surface phenomenon. However, an alteration of surface states may alter internal dislocation structures to establish a new stress balance in the specimen, even when hydrogen is absent. The observations may not rule out surface effects on the apparent dislocation activities.

Enhanced strain localization is another feature of hydrogen effects. In situ observations revealed the crack propagation associated with the emission of dislocations from the crack tips in iron foil [41]. The generation of dislocations in the vicinity of dislocation cell walls was also observed ahead of the crack tip. Initially formed and arrested cracks in a vacuum restarted when hydrogen gas was introduced into the environmental cell, even at a stress lower than in a vacuum. Deformation was highly localized near the crack tip and resulted in the formation of small voids. The observations have served as an experimental basis for the hydrogen-enhanced localized plasticity (HELP) mechanism of hydrogen embrittlement described in the following Sects. 5.5 and 10.2.

Hydrogen fugacity in the environment cell was much lower than the threshold fugacity at stress relaxation for carbon steel [25]. Concentrations of solute hydrogen estimated from Sieverts' law are very low compared with other alloying elements or impurities that alter the deformation behaviors of steels. Accordingly, direct interactions of hydrogen with moving dislocations are hardly viable to enhance dislocation mobility. On the other hand, most dislocation arrays observed by TEM are initially pinned at the surface of the foil specimen, suppressing their movements. It is feasible that a substantial decrease in the surface energy caused by hydrogen adsorption, as shown in Fig. 5.8, releases pinning and alters the mechanical balance to move dislocations.

5.5 Elastic and Atomistic Calculations

5.5.1 Elastic Shielding of Stress Centers

The elastic interaction energy between a hydrogen atom and an edge dislocation, originating in the volumetric effect, is described in Sect. 3.1.2. Hydrogen-enhanced dislocation mobility revealed by in situ TEM is quite general for fcc, bcc, and hcp crystal structures and also for both edge and screw types of dislocations. In addition to some qualitative explanations of experimental observations described in Sect. 5.2.3, quantitative estimation in a frame of elasticity has been made about reducing barriers for dislocation motion.

The mobility of dislocations is affected by elastic interactions between dislocations and also between dislocations and other stress centers, such as solute atoms and precipitates. Hydrogen atmospheres form in the dilatational fields to make the energy of the system minimum. Sofronis and Birnbaum calculated hydrogen effects on the dislocation mobility, considering both the first-order dilatational interaction energy, expressed by Eq. (3.8) for an edge dislocation, and a second-order interaction energy that arises from the change in the elastic moduli caused by hydrogen in solid solution [38, 42].

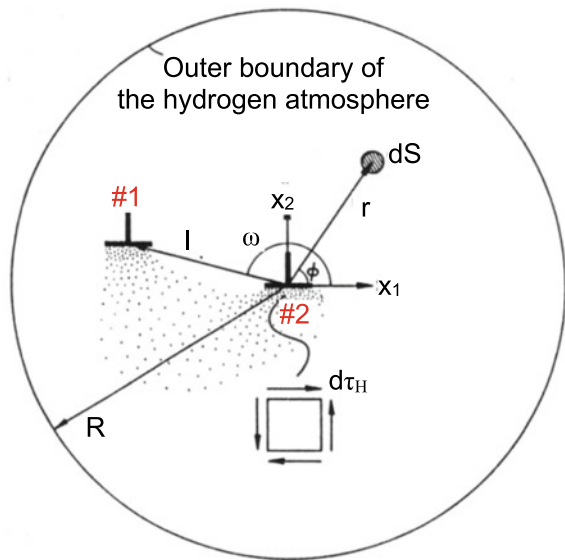
Calculations were made for various configurations and types of elastic centers. Figure 5.9 [38, 42] is a schematic illustration of the coordinates of interacting two edge dislocations of the same sign and hydrogen atmosphere. The shear stress acting at the core of dislocation #2 located at the center is the sum of shear stresses due to the hydrogen atmosphere and neighboring dislocation #1.

The hydrogen atmosphere in the area dS exerts the shear stress $d\tau_H$. Regarding the hydrogen volumetric effect, the net shear stress, τ_H , acting at dislocation #2 due to the hydrogen atmosphere of the local concentration $C(r, \varphi)$ is

$$\tau_H = -\frac{\mu}{2\pi(1-\nu)} \frac{V_H}{N_A} \int_0^{2\pi} \int_{r_2}^R C(r, \varphi) \frac{\sin 2\varphi}{r} dr d\varphi, \quad (5.12)$$

where μ is the shear modulus, V_H is the partial molar volume of hydrogen, N_A is Avogadro's number, r_2 is the inner cut-off radius of dislocation #2, and R is the outer cut-off radius of the atmosphere centered at dislocation #2. $C(r, \varphi)$ is the hydrogen distribution in equilibrium with an applied stress field and stress fields arising from dislocations #1 and #2. On the other hand, the shear stress τ_D resolved along the slip

Fig. 5.9 Schematic model for the shear stress acting at the core of dislocation #2 by the hydrogen dilatation lines of an infinitesimal area dS at the position (r, φ) (Birnbaum et al. [38])



plane and exerted by dislocation #1 is

$$\tau_D = -\frac{b_1}{2\pi(1-\nu)} \frac{\cos \omega \cos 2\omega}{l}, \quad (5.13)$$

where b_1 is the Burgers vector of dislocation #1. The net shear stress exerting at the core of dislocation #2 is equal to $\tau_D + \tau_H$.

Figure 5.10 [38, 42] plots calculated normalized shear stresses, τ_H/μ , τ_D/μ , and $(\tau_D + \tau_H)/\mu$, versus normalized distance, l/b , and nominal hydrogen concentrations of $H/M = 0.1$ and 0.01 for bcc niobium at 300 K. Figure 5.10 indicates that the hydrogen atmosphere reduces the repulsive interaction between parallel edge dislocations of the same sign at a close distance. Two dislocations of opposite signs also give very similar results. Calculated elastic energies of edge dislocations with and without hydrogen atmospheres are shown in Fig. 5.11 [39] for aluminum as a function of nominal hydrogen concentration. The energies are expressed as the energy per atomic distance along the dislocations.

In both Figs. 5.10 and 5.11, substantially high hydrogen concentrations over 0.01 are necessary to exhibit the shielding effects of hydrogen. Ferreira et al. postulated that the formation of hydrogen atmosphere around edge components of dislocations decreased the system's energy and disturbed cross-slipping [39]. However, low hydrogen gas pressure in the environmental cell is unlikely to realize such a high hydrogen concentration.

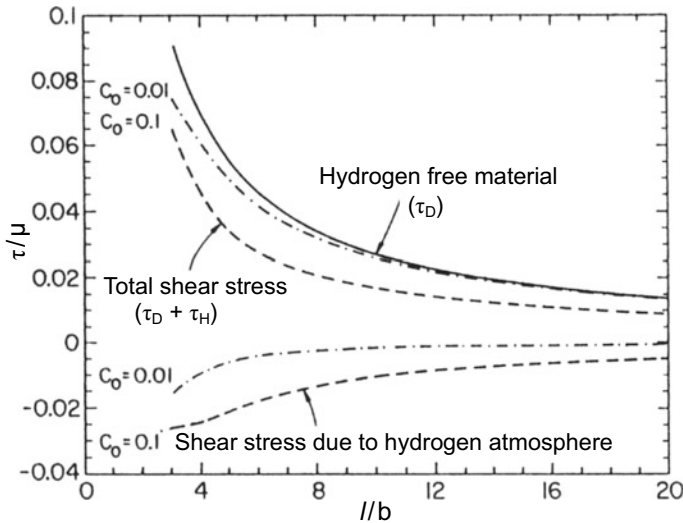
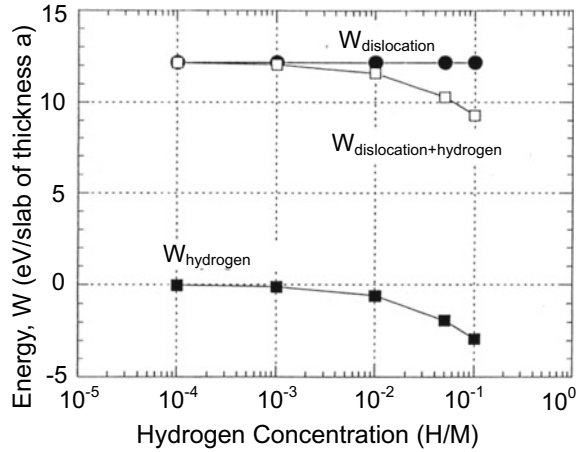


Fig. 5.10 Normalized shear stress due to hydrogen, τ_H/μ , and due to dislocation #1, τ_D/μ , and net shear stress, $(\tau_D + \tau_H)/\mu$, at the core of dislocation #2 at 200 K and nominal hydrogen concentrations of $H/M = 0.1, 0.01$ in Nb (Sofronis et al. [42])

Fig. 5.11 Calculated elastic energies of edge dislocations with and without hydrogen atmospheres as a function of hydrogen concentrations. The energies are given as energy per atomic distance along the dislocation. (Ferreira et al. [39])



For screw dislocations, direct interactions with hydrogen are very weak because of a cubic symmetry of the deformation field around a hydrogen atom. Sofronis and Birnbaum showed that hydrogen shielding also operates in elastic interactions between dislocations and a carbon atom. Screw dislocations interact with carbon atoms. Then, the stress acting on screw dislocations as well as edge dislocations are affected by hydrogen resulting from interactions between hydrogen and carbon atoms [38, 42]. Sofronis and Birnbaum calculated the interaction energy between a dislocation and a carbon atom in the hydrogen atmosphere. A finite element method calculation was conducted, taking into account the modulus changes of the carbon atom by hydrogen atmosphere using data for niobium [43],

$$E = E_0(1 + 0.34c), \quad \nu = \nu_0 - 0.025c, \quad \mu = \mu_0 \frac{1 + 0.34c}{1 - 0.0177c}. \quad (5.13)$$

The results are complicated; either an increase or decrease in the interaction energy, depending on the locations and tetragonal axes of the carbon atom. The modulus effect is a weak second-order interaction operating in a short range. Hydrogen effects were prominent when the carbon atom locates very close, within one Burgers vector, to the dislocation core. Also, the calculations were for the case of a very high nominal hydrogen concentration of $H/M = 0.1$.

On the other hand, hydrogen softening is not feasible for the movement of edge dislocations. Atomistic modeling for the edge dislocation mobility and pileups showed hydrogen effects against the shielding of elastic fields [44]. Large-scale molecular dynamics simulations were conducted by applying shear stress to a cell composed of bcc iron and three edge dislocations with/without hydrogen precharging. The Cottrell atmosphere of hydrogen forms around moving dislocations, and hydrogen does not affect the pileup structures. The results imply that the drag of hydrogen reduces the mobility of edge dislocation and that the hydrogen atmosphere provides no measurable shielding of dislocation interactions.

5.5.2 Mobility of Screw Dislocations—Atomistic Calculations

First-principles calculations of the hydrogen binding energy with the screw dislocation core are described in Sect. 3.1.2. The nucleation of the kink pair and its expansion control the movement of a screw dislocation. Wen et al. simulated the effects of hydrogen on the nucleation and the sideward movement energies of kink pairs in bcc iron [45]. Assuming that a kink nucleates on $1/2[111]$ screw dislocation at a hydrogen atom, the hydrogen binding energies were calculated for various sites of hydrogen in the core. The activation energy of kinking was expressed as the maximum of the increased energy of the dislocation during kinking. When a kink pair meets hydrogen during expansion, the sideward motion of the kink pair is impeded by hydrogen. The kinking process was determined to take the minimum energy path during expanding along the dislocation meeting and overcoming another hydrogen atom.

Softening by hydrogen, i.e., a reduction in the activation energy, appeared in the sideward movement rather than in the nucleation of a kink pair when the hydrogen state changed from a weaker trapped site to a stronger one. The maximum reduction by hydrogen was about 20% of the overall increase, about 100 kJ/mol, in the dislocation energy during the kinking process. However, softening was not always the case in the kinking process. Hardening was expected when the transition was from a stronger to a weaker trapped site. When hydrogen binding energies were the same before and after kinking, hydrogen effects did not appear in kinking. The sideward motion of a kink pair is impeded when the kink pair meets hydrogen, thus inducing hardening.

Itakura et al. conducted a density functional theory (DFT) calculation of the kink-pair nucleation enthalpy H_k in bcc iron, using a line tension model of a curved dislocation with/without hydrogen [46]. Two types of the core configuration, stable and unstable, were assumed for a screw dislocation, and hydrogen atoms were placed at various interstitial T -sites near the core. The movement of a screw dislocation tolerates alternation of the two core configurations with the saddle point of the migration path close to the unstable configuration. The enthalpy of a curved dislocation incorporates the position energy of the core, the Peierls barrier, the contributions of external stress, and the interaction energy between the dislocation line and hydrogen atoms. A reduction in H_k by hydrogen enhances the kink nucleation rate. The calculated H_k was a function of applied stress, decreasing from 700 kJ/mol to zero as shear stress up to 1000 MPa was applied [46]. The reduction of H_k by hydrogen was about 11 kJ/mol for all applied stress levels. The kink nucleation rate determined the velocity of a screw dislocation. For softening to occur, sufficient hydrogen trapping must occur at moving kinks. On the other hand, hydrogen trapping at a kink disturbs the kink movement.

Itakura et al. imposed four conditions for hydrogen softening to occur [46]: (1) the upper limit of temperature, T_U , for a sufficient hydrogen concentration, (2) the lower limit of the applied stress, σ_L , to overcome kink trapping by hydrogen, (3) an upper limit of the applied stress, σ_{U1} , above which dislocation velocity is too

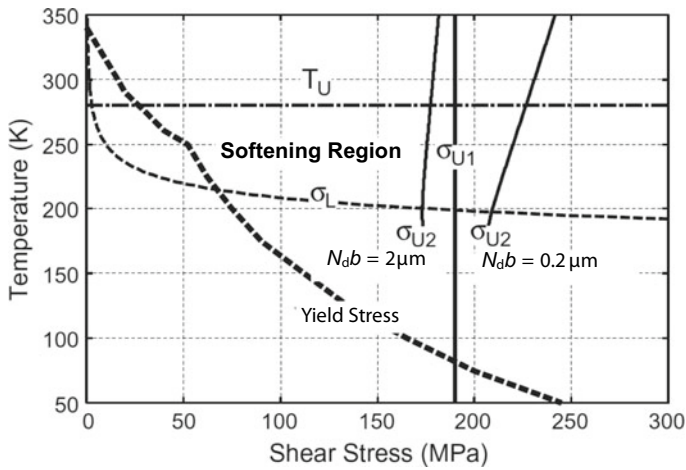


Fig. 5.12 Region in the temperature-stress diagram where an increase in the screw dislocation velocity by solute hydrogen is possible. N_d Dislocation length in unit of b . Calculation for 0.1 at. ppm of hydrogen and two dislocation lengths of 2.0 and 0.2 μm (Itakura et al. [46])

fast, and (4) an upper limit of the applied stress, σ_{U2} , above which the increasing velocity of a kink cancels kink trapping by hydrogen. Figure 5.12 shows a region in the temperature-stress diagram where the screw dislocation velocity increases by hydrogen in bcc iron for the bulk hydrogen concentration which is 0.1 at. ppm [46]. Values of σ_{U2} were calculated for two typical dislocation lengths denoted as N_d in the unit of the Burgers vector b . The temperature ranges are almost consistent with observed flow stress behaviors in Sect. 5.2, while exact hydrogen concentrations are not definite.

Section 3.2 describes the generation of vacancies associated with dragging jogs on screw dislocations and its enhancement by hydrogen. The velocity of jog under applied stress is a function of the sum of the formation and the migration energies of vacancies. Matsumoto et al. noticed that hydrogen effects on the two energies almost cancel, and the velocity of jogs is not affected by the presence of hydrogen [47]. Hydrogen effects on jog dragging increase the density of created vacancies by suppressing the diffusion of vacancies.

Teheranchi et al. remarked on an indirect function of hydrogen on the flow stress in nickel, i.e., hydrogen effects on dislocation–solute interactions, instead of the double-kink nucleation mechanism [48]. The field of solute atoms interacts with dislocations, and hydrogen modifies the misfit strain tensor of the solute. Teheranchi et al. addressed the glide of an edge dislocation through randomly distributed solutes in a nickel matrix. Molecular dynamics simulations were conducted to estimate the flow stress for two systems with identical spatial distributions of either solutes or solute–hydrogen complexes. Simulations using vacancies as the solutes showed reduced (softening) glide stress when hydrogen is bound to vacancies.

However, calculations were for high vacancy and vacancy-hydrogen complex concentrations of the order of %. On the other hand, for carbon and sulfur atoms as solutes, their complexes with hydrogen have larger misfit strains, indicative of hydrogen-induced hardening rather than softening.

References

1. H.A. Wriedt, R.A. Oriani, *Scr. Metall.* **8**, 203–208 (1974)
2. N.E. Paton, O. Buck, J.C. Williams, *Scr. Metall.* **9**, 687–691 (1975)
3. E. Lunarska, A. Zielinski, M. Smialowski, *Acta Metall.* **25**, 305–308 (1977)
4. S. Matsuyama, in *Report of Studies on the Mechanism of Delayed Fracture* (Iron and Steel Institute Japan, Tokyo, 1975), pp. 113–124
5. A. Goumelon, *Mem. Sci. Rev. Mét.* **72**, 475–489 (1975)
6. A. Kimura, H. Matsui, H. Kimura, Hydrogen in metals. *Suppl. Trans. JIM* **21**, 541–544 (1980)
7. M. Cornet, S. Talbot-Besnard, Hydrogen in metals. *Suppl. Trans. JIM* **21**, 545–548 (1980)
8. Y. Tobe, W.R. Tyson, *Scr. Metall.* **11**, 849–852 (1977)
9. I.M. Bernstein, *Scr. Metall.* **8**, 343–350 (1974)
10. S. Asano, Y. Nishino, M. Otsuka, *Jpn. Inst. Metals* **43**, 241–248 (1979)
11. S. Moriya, H. Matsui, H. Kimura, *Mater. Sci. Eng.* **40**, 217–225 (1979)
12. H. Matsui, H. Kimura, S. Moriya, *Mater. Sci. Eng.* **40**, 207–216 (1979)
13. H. Kimura, H. Matsui, A. Kimura, Hydrogen in metals. *Suppl. Trans. JIM* **21**, 533–540 (1980)
14. H. Matsui, H. Kimura, A. Kimura, *Mater. Sci. Eng.* **40**, 227–234 (1979)
15. H. Wada, S. Sakamoto, Hydrogen in metals. *Suppl. Trans. JIM* **21**, 553–556 (1980)
16. R.A. Oriani, P.H. Josephic, *Metall. Trans. A* **11A**, 1809–1820 (1980)
17. E. Lunarska, V. Novak, N. Zarubova, S. Kadeckova, *Scr. Metall.* **17**, 705–710 (1983)
18. C.G. Park, K.S. Shin, J. Nakagawa, M. Meshii, *Scr. Metall.* **14**, 279–284 (1980)
19. C.D. Beachem, *Metall. Trans.* **3**, 437–451 (1972)
20. E. Furubayashi, *J. Phys. Soc. Jpn* **27**, 130–140 (1969)
21. A.S. Keh, *Phil. Mag.* **12**, 9–30 (1965)
22. W.G. Johnston, J.J. Gilman, *J. Appl. Phys.* **30**, 129–144 (1959)
23. I. Gupta, J.C.M. Li, *Metall. Trans.* **1**, 2323–2330 (1970)
24. E. Lunarska, *Scr. Metall.* **11**, 283–287 (1977)
25. R.A. Oriani, P.H. Josephic, *Acta Metall.* **27**, 997–1005 (1979)
26. M. Nagumo, T. Tamaoki, T. Sugawara, in *Hydrogen Effects on Materials Behavior and Corrosion Deformation Interactions*, ed. by N.R. Moody, A.W. Thompson, R.E. Ricker, C.W. Was, K.H. Jones (TMS, Warrendale PA, 2003), pp. 999–1008
27. T. Fujita, T. Sakai, in *Report of Studies on the Mechanism of Delayed Fracture* (Iron and Steel Institute Japan, Tokyo, 1975), pp. 189–199
28. M. Nagumo, Y. Monden, in *Report of Studies on the Mechanism of Delayed Fracture* (Iron Steel Institute Japan, Tokyo, 1975), pp. 149–164
29. A.H. Cottrell, *Dislocations and Plastic Flow in Crystals*, Chap. 16 (Oxford University Press, London, 1956), pp. 195–215
30. A.H. Cottrell, *Phil. Mag. Lett.* **82**, 65–70 (2002)
31. R.A. Oriani, P.H. Josephic, *Acta Metall.* **29**, 669–674 (1981)
32. Z.R. Xu, R.B. McLellan, *Acta Mater.* **46**, 4543–4547 (1998)
33. R.W. Revie, H.H. Uhlig, *Acta Metall.* **22**, 619–627 (1974)
34. D.A. Jones, *Metall. Trans. A* **16A**, 1133–1141 (1985)
35. N.J. Petch, *Phil. Mag.* **1**, 331–337 (1956)
36. H.K. Birnbaum, C. Buckley, F. Zeides, E. Sirois, P. Rozenak, S. Spooner, J.S. Lin, *J. Alloys Compounds* **253–254**, 260–264 (1997)

37. T. Tabata, H.K. Birnbaum, *Scr. Metall.* **17**, 947–950 (1983)
38. H.K. Birnbaum, P. Sofronis, *Mater. Sci. Eng.* **A176**, 191–202 (1994)
39. P.J. Ferreira, I.M. Robertson, H.K. Birnbaum, *Acta Mater.* **47**, 2991–2998 (1999)
40. I.M. Robertson, H.K. Birnbaum, *Acta Metall.* **34**, 353–366 (1986)
41. T. Tabata, H.K. Birnbaum, *Scr. Metall.* **18**, 231–236 (1984)
42. P. Sofronis, H.K. Birnbaum, *J. Mech. Phys. Solids* **43**, 49–90 (1995)
43. F.M. Mozzolai, H.K. Birnbaum, *J. Phys. F: Met. Phys.* **15**, 507–523 (1985)
44. J. Song, W.A. Curtin, *Acta Mater.* **68**, 61–69 (2014)
45. M. Wen, S. Fukuyama, K. Yokogawa, *Acta Mater.* **51**, 1767–1773 (2003)
46. M. Itakura, H. Kaburaki, M. Yamaguchi, T. Okita, *Acta Mater.* **61**, 6857–6867 (2013)
47. R. Matsumoto, N. Nishiguchi, S. Taketomi, N. Miyazaki, *J. Soc. Mater. Sci. Jpn.* **63**, 182–187 (2014)
48. A. Tehranchi, B. Yin, W.A. Curtin, *Phil. Mag.* **97**, 400–418 (2017)